Measuring thermal expansion using X-band Persistent Scatterer Interferometry

Michele Crosetto [1,*], Oriol Monserrat [1], María Cuevas-González [1], Núria Devanthéry [1], Guido Luzi [1] and Bruno Crippa [2]

[1] Institute of Geomatics, Av. Gauss 11, E-08860, Castelldefels (Barcelona), Spain; michele.crosetto@ideg.es; oriol.monserrat@ideg.es; maria.cuevas@ideg.es; nuria.devanthery@ideg.es; guido.luzi@ideg.es

[2] Department of Earth Sciences, University of Milan, Via Cicognara 7, I-20129, Milan, Italy; bruno.crippa@unimi.it

* Author to whom correspondence should be addressed; e-mail: michele.crosetto@ideg.es; Tel.: +34-93-556-9294; Fax: +34-93-556-9292

Abstract:

This paper is focused on the estimation of the thermal expansion of buildings and infrastructures using X-band Persistent Scatterer Interferometry (PSI) observations. For this purpose an extended PSI model is used, which allows separating the thermal expansion from the total observed deformation thus generating a new PSI product: the map of the thermal expansion parameter, named thermal map. The core of the paper is devoted to the exploitation of the information contained in the thermal maps: three examples are discussed in detail, which concern a viaduct, a set of industrial buildings and two skyscrapers. The thermal maps can be used to derive the thermal expansion coefficient of the observed objects and information on their static structure. In addition, the paper illustrates the distortions in the PSI deformation products that occur if the thermal expansion is not explicitly modelled. Finally, an inter-comparison exercise is described, where the thermal expansion coefficients estimated by PSI are compared with those derived by a Ku-band ground-based SAR campaign.

Keywords: thermal expansion; very high resolution imagery; SAR; TerraSAR-X, ground-based SAR.

---

1. Introduction

The Persistent Scatterer Interferometry (PSI) technique (Ferretti et al., 2000) has proven to be an effective tool to measure deformations from which numerous disciplines have benefited. They include applications related to tectonics (Musson et al., 2004; Bürgmann et al., 2006),

volcanoes (Salvi et al., 2004), landslides (Hilley et al., 2004), land subsidence caused by groundwater pumping and mining (Tomás et al., 2005; Bell et al., 2008; Colesanti et al., 2005), and urban monitoring (Crosetto et al., 2008).

One of the main advantages of PSI is its sensitivity to small deformations. Several validation experiments have shown this property for C-band PSI. Ferretti et al. (2007) show sub-millimeter accuracy with an experiment based on dihedral reflectors. In the PSIC4 project, the inter-comparison of deformation velocities estimated by different teams yielded standard deviations that range from 0.6 to 1.86 mm/yr (Raucoules et al., 2009). Another inter-comparison experiment, from the Terrafirma Validation project, gave standard deviations of the velocities that range from 0.45 to 0.66 mm/yr (Crosetto et al., 2007).

With the advent of X-band data, PSI has experienced a further improvement of its sensitivity to deformations, e.g. see Crosetto et al. (2010). The sensitivity is so high that the interferometric phases (i.e. the main PSI observations) often contain a non negligible component related to thermal expansion, i.e. PSI senses the displacements that are caused by temperature differences in the imaged area between SAR acquisitions. It is worth noting that this has also been reported in some C-band PSI studies, e.g. Ferretti et al. (2005), Perissin and Rocca (2006) and Crosetto et al. (2008). However, these results are often related to the deformation time series of single Persistent Scatterers (PSs), while with X-band PSI the thermal expansion is evident over large sets of PSs. This makes possible the analysis and interpretation of the thermal expansion signal of single objects like buildings, bridges, etc. (Monserrat et al., 2011; Fornaro et al., 2013).

The X-band PSI capability of sensing the thermal expansion, which is illustrated in the following sections, represents a powerful argument to promote this satellite-based deformation monitoring technique. However, it has an important disadvantage: the total observed deformation contains both the thermal expansion and the deformation signal of interest. Note that in deformation analysis what usually matters is the total observed deformation without

thermal expansion effects. For this reason, in order to derive proper deformation estimates, the two components have to be separated. Note that the same problem occurs in many other high-precision deformation monitoring techniques, e.g. see Dong et al. (2002). This paper discusses two main issues related to thermal expansion: how to separate the thermal expansion from the total deformation and how to exploit the information related to the thermal expansion. The first issue is addressed in the following section, which describes an extended model for X-band PSI. This model generates a new PSI product: the so-called thermal maps. This is followed by a section which provides a discussion and the interpretation of three examples of thermal maps: a viaduct, a set of industrial buildings and two skyscrapers. Then an inter-comparison exercise is described, where the thermal expansion coefficients estimated by PSI are compared with those derived by Ku-band Ground-Based SAR (GBSAR) data. Finally, the conclusions of this paper are summarized.

2. An extended model for X-band PSI

In this section we briefly discuss how the thermal expansion component can be properly modelled and estimated starting from X-band PSI interferometric phases, Φ, see Monserrat et al. (2011). This estimation requires an extension of the classical two-parameter PSI model (deformation velocity, v, and residual topographic error, RTE), by including a thermal expansion parameter, which is related to the average temperature differences between the acquisition of the images. The extended model is:

$$\Delta\Phi_e^k = \frac{4\pi}{\lambda}\Delta T^k \Delta v_e + \frac{4\pi}{\lambda}\frac{B_\perp^k}{R_e^k sen\theta_e^k}\Delta RTE_e + \frac{4\pi}{\lambda}\Delta Temp^k \Delta Th_e + \Delta\Phi res_e^k$$

where:

- $\Delta\Phi_e^k$ is the differential interferometric wrapped phase, where k is the interferogram number, e the edge that connects two PSs and Δ indicates the difference of the phases of the two PSs.

- The first component is the deformation velocity component, where Δv_e is the unknown differential velocity associated with e, ΔT^k is the temporal baseline of interferogram k and λ is the radar wavelength.
- The second component is the *RTE* component, where ΔRTE_e is the differential *RTE* associated with e, while $B_\perp^k$, R_e^k and θ_e^k are the normal baseline, the slant range and incidence angle of interferogram k, respectively.
- The third component is the thermal expansion component, where $\Delta Temp^k$ is the temperature difference at the time of acquisition of the two images of interferogram k and ΔTh_e is the differential thermal expansion parameter associated with e. We use an average air temperature for each image, which is considered constant through the entire imaged scene.
- The last term, $\Delta\Phi res_e^k$, is the residual phase component.

By integrating the ΔTh_e values over the whole set of edges that connect the PSs, a new PSI product is obtained: the map of the thermal expansion parameter, hereafter called thermal map. The precision achievable in the estimation of this parameter is discussed in Monserrat et al. (2011) and Fornaro et al. (2013). The former reference reports a standard deviation σ_{Th} of 0.04 mm/◦C, which was estimated over homogeneous portions of the runways of an airport.

Alternatively to the above model, other approaches have been proposed in the literature, which make use of a seasonal sinusoidal deformation model (Gernhardt et al., 2010; Duro et al., 2010). However, the above model is more accurate because it explicitly makes use of the temperature, thus avoiding the hypothesis of a sinusoidal temporal evolution. The above equation can be used to model and separate the linear deformation from the thermal expansion component. However, this can be accomplished only if the three parameters can be properly estimated. This aspect basically depends on the number of available SAR images (the larger,

the better) and the correlation (the lower, the better) between these three vectors: [ΔT^k], [$B_\perp^k$], [$\Delta Temp^k$], with k varying from 1 to the Nth available interferogram.

3. Application of the extended model

This section provides the discussion and interpretation of three different applications of the extended model. They concern different types of structures that can be found in an urban and peri-urban environment: a viaduct, a set of industrial buildings and two skyscrapers.

3.1 Thermal map over a viaduct

This section describes the first example of thermal map, which concerns a viaduct, see Fig. 1. This structure shows a periodic pattern, which is clearly visible in single interferograms (Fig. 1a). Using 27 StripMap TerraSAR-X images and 51 interferograms, which cover the period December 2007 to November 2009, the extended model was used to analyse this structure. Fig. 1b shows the deformation velocity map, which indicates that the structure is stable. Fig. 1c shows the corresponding thermal map, while Fig. 1d shows an enlargement of this map. These two maps clearly display a periodic pattern, with 96 m, that corresponds to the locations of the thermal joints of the viaducts, which are highlighted by white squares in Fig. 1d. Between two subsequent joints, the thermal map has values that range approximately from -0.35 to +0.3 mm/ºC. This makes a total difference of 0.65 mm/ºC, which is observed along the satellite Line-Of-Sight (LOS) direction. Assuming that this is caused by horizontal thermal expansion along the main bridge direction and for a length of 96 m, this corresponds to an estimated coefficient of linear thermal expansion of $11.7 \cdot 10^{-6}$/ºC, which is typical for reinforced concrete, e.g. see Merritt et al. (1976). The interpretation of the result from Fig. 1c and 1d involves three basic properties of the viaduct: the material and hence the thermal expansion coefficient, the geometry and the static structure. Fig. 2 shows a scheme of the viaduct, where the geometry was derived from Google Earth and the static structure was inferred directly from

the thermal expansion map: it includes a pinned joint and three slider joints. The white arrows indicate the vertical and horizontal components of the parameter *Th* in correspondence of the four supports, while the black arrows show the sum of the above components projected in the LOS direction. The above components were computed from the static scheme and using the coefficient of linear thermal expansion of $11.7 \cdot 10^{-6}$/ºC. The static scheme was validated by an in situ inspection of the viaduct.

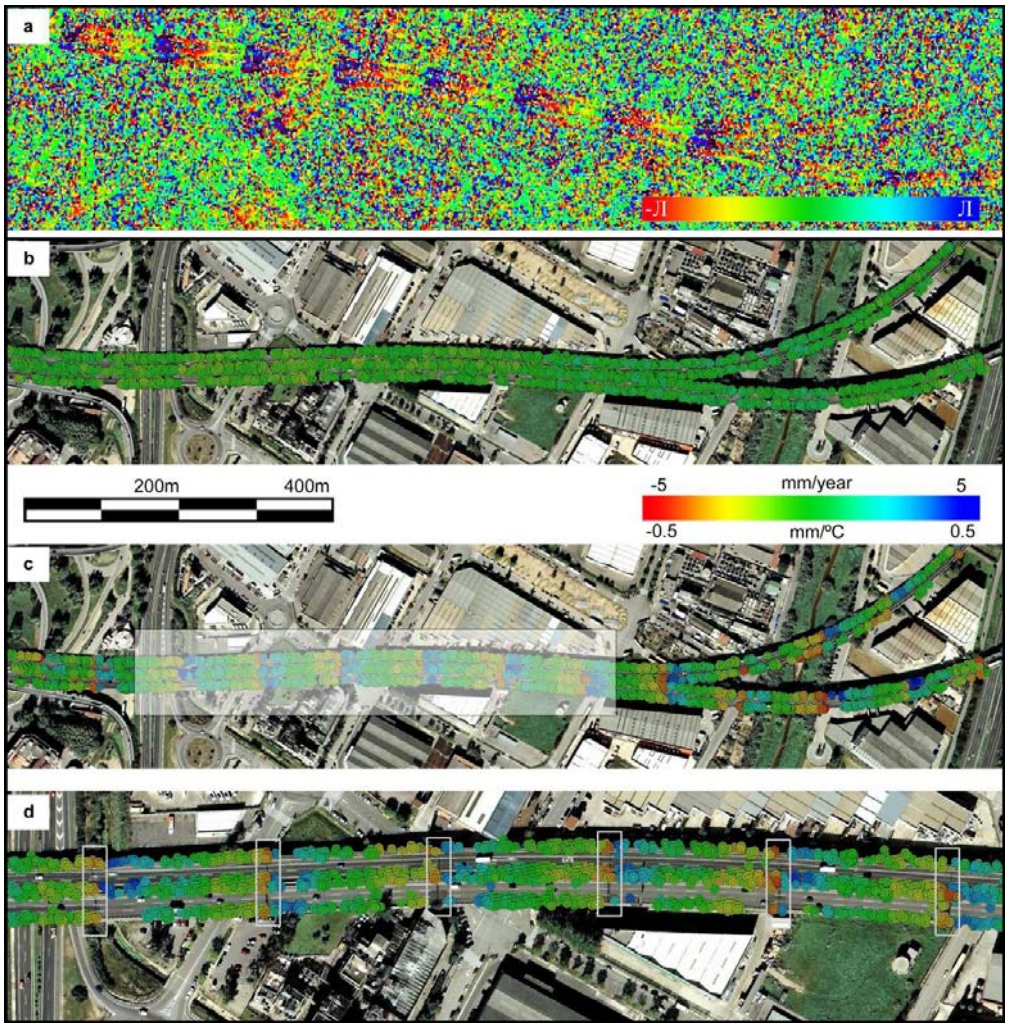

Fig. 1. Interferogram of the analysed viaduct, located in Montmeló (Barcelona, Spain), which covers the period from 4 July 2008 to 20 February 2009 (a). Geocoded deformation velocity map (b), thermal map (c) and zoom over the rectangle shown in c (d). The white squares shown in d indicate the positions of the viaduct expansion joints. The maps are superimposed over a Google Earth image (© 2013 Google, Institut Cartogràfic de Catalunya).

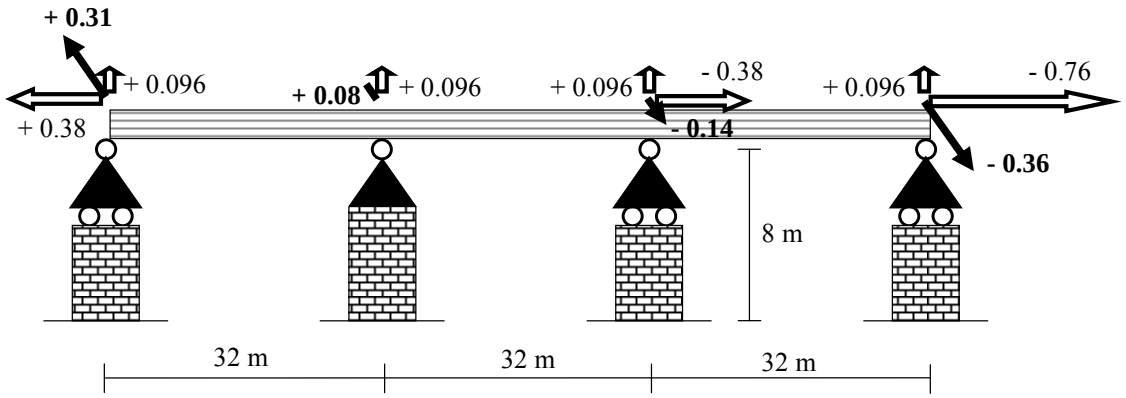

Fig. 2. Scheme of a 96-m section of the viaduct, which is limited by a pair of thermal joints. The scheme includes four supports: a pinned joint (2nd support from left) and three slider joints. The white arrows indicate the vertical and horizontal components of the thermal expansion parameter, Th, while the black arrows represent their projection in the Line-Of-Sight direction. All values, with exception of those of the geometry that are expressed in [m], are in [mm/ºC].

One may notice that the LOS values of Th estimated from the static scheme, which range between -0.36 and +0.31 mm/ºC, are very close to those estimated from satellite and shown in Fig. 1c and 1d: this confirms that the scheme from Fig. 2 summarizes well the basic properties of the viaduct, and in particular its coefficient of thermal expansion and the structural static scheme. Another example of PSI thermal expansion study over a viaduct can be found in Fornaro et al. (2013).

3.2 Thermal map over industrial buildings

The second example concerns a set of industrial buildings located in Barcelona (Spain). Fig. 3a shows an orthoimage of the area at hand. In this case the PSI analysis was performed using 13 StripMap TerraSAR-X images, covering the period December 2007 to September 2008. Fig. 3b shows the velocity map estimated with the classical two-parameter PSI model: strong deformation patterns, with deformation velocities ranging from -20 to +20 mm/yr, are visible.

This result differs substantially from the velocity map estimated using the extended PSI model, see Fig. 3d. The difference reflects the effect of thermal expansion, which is not modelled in Fig. 3b and, as a consequence, generates distortions in the velocity map, thus creating a kind of "virtual displacement rates". By contrast, when the thermal expansion component is properly modelled it generates a much more accurate deformation velocity map and, in addition, the thermal map is obtained, see Fig. 3c.

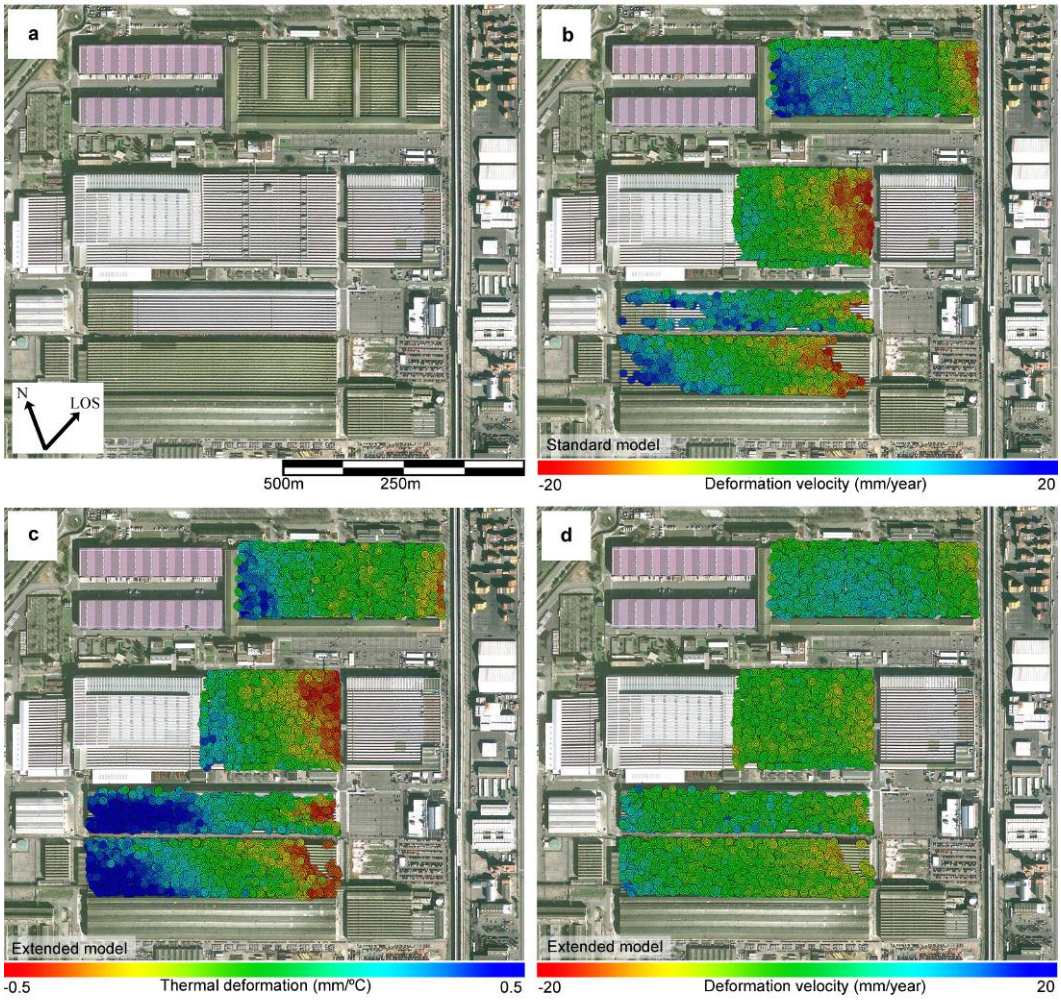

Fig. 3. Orthoimage of the observed industrial area (a). Geocoded deformation velocity map estimated using the standard PSI model (b). Thermal map (c) and deformation velocity map (d) estimated with the extended PSI model. The maps are superimposed over a Google Earth image (© 2013 Google, Institut Cartogràfic de Catalunya).

This example is useful to illustrate the importance of properly modelling thermal expansion: if this is not performed, the PSI end users should be warned on the risk of obtaining deformation products that potentially contain spurious patterns due to unmodelled thermal expansion effects. Note that this risk increases if the PSI products are derived from PSI datasets that cover short periods e.g. of several months. It is worth noting that the velocity map shown in Fig. 3d still shows a residual thermal pattern: this is due to the limited PSI dataset that does not allow the velocity to be perfectly separated from the thermal parameter. The thermal map shown in Fig. 3c displays values that range approximately between -0.6 and +0.5 mm/ºC. These values reflect the displacements of the roofs of the analysed buildings. Note that the pattern that is visible in the thermal map is directly related to the LOS direction, which is indicated in Fig. 3a.

3.3 Thermal map over two skyscrapers

The results discussed in this section concern two skyscrapers observed with two datasets: 28 StripMap TerraSAR-X (TSX) images and 56 interferograms spanning the period December 2007 to November 2009, and 16 StripMap CosmoSkyMed (CSM) images and 47 interferograms spanning the period July 2010 to November 2011. The skyscraper on the left side is named S_A and the other S_B.

Let's discuss the results of S_B. Fig. 4a and 4b show the deformation velocity maps estimated using the classical two-parameter PSI model. It is interesting to note the different distortions induced in these two maps when the classical PSI model is used. The map obtained from CSM shows a strong deformation pattern: this is clearly caused by thermal effects because it disappears when the extended model is employed, see Fig. 4c. The result from TSX is very different: in fact, there are almost no PSs over S_B. This difference is related to the issue of estimability mentioned in Section 2. With the CSM dataset, the vectors $[\Delta T^k]$ and $[\Delta Temp^k]$ are strongly correlated and this results in a velocity map that is strongly distorted by the thermal expansion. By contrast, in the TSX dataset, which almost doubles the number of SAR

images, these two vectors are much less correlated, preventing the corruption of the velocity map by the thermal expansion, which, however, remains as an unmodelled term. This has a direct impact on the temporal model coherence, which is the goodness-of-fit parameter used to measure the quality of the modelling (Ferretti et al., 2001). In the case of CSM this parameter is quite high, and hence the PSs are accepted, while in the case of TSX it is low and the PSs are rejected (the used threshold was 0.6). Fig. 4c and 4d show the deformation velocity maps estimated with the extended model and both indicate stability. Finally, Fig. 4e and 4f show the thermal maps, with values that roughly range from 0 to +1 mm/ºC.

It is worth noting that the behaviour of S_A slightly differs from that of S_B: the thermal expansion parameter Th is sensibly lower. In the estimation based on the TSX dataset, which is the more reliable, the Th values approximately range between 0 mm/ºC and 0.55 mm/ºC, while in the neighbour skyscraper, which has exactly the same height, these values reach 1 mm/ºC. This difference is probably due to the different static structure of the two skyscrapers: for S_B the main structure is, at least partially, external and hence directly exposed to the seasonal temperature changes. In contrast, for S_A these changes can be more moderate due to the fact that its main static structure is internal, i.e. not directly exposed to the seasonal temperature changes.

The reduced magnitude of Th values of S_A is reflected in Fig. 4b, where the velocity map is correctly estimated even using the two-parameter model. A similar result is shown in Fig. 4a, even though it is noisier. Finally, it is worth noting that the CSM solution (both velocity and thermal maps) for S_A is slightly different from the homologous TSX solution. For instance, the CSM thermal values are slightly overestimated with respect to the TSX ones. This is caused by the limited size of the CSM dataset, which does not allow us to correctly separate the deformation velocity from the thermal expansion parameter.

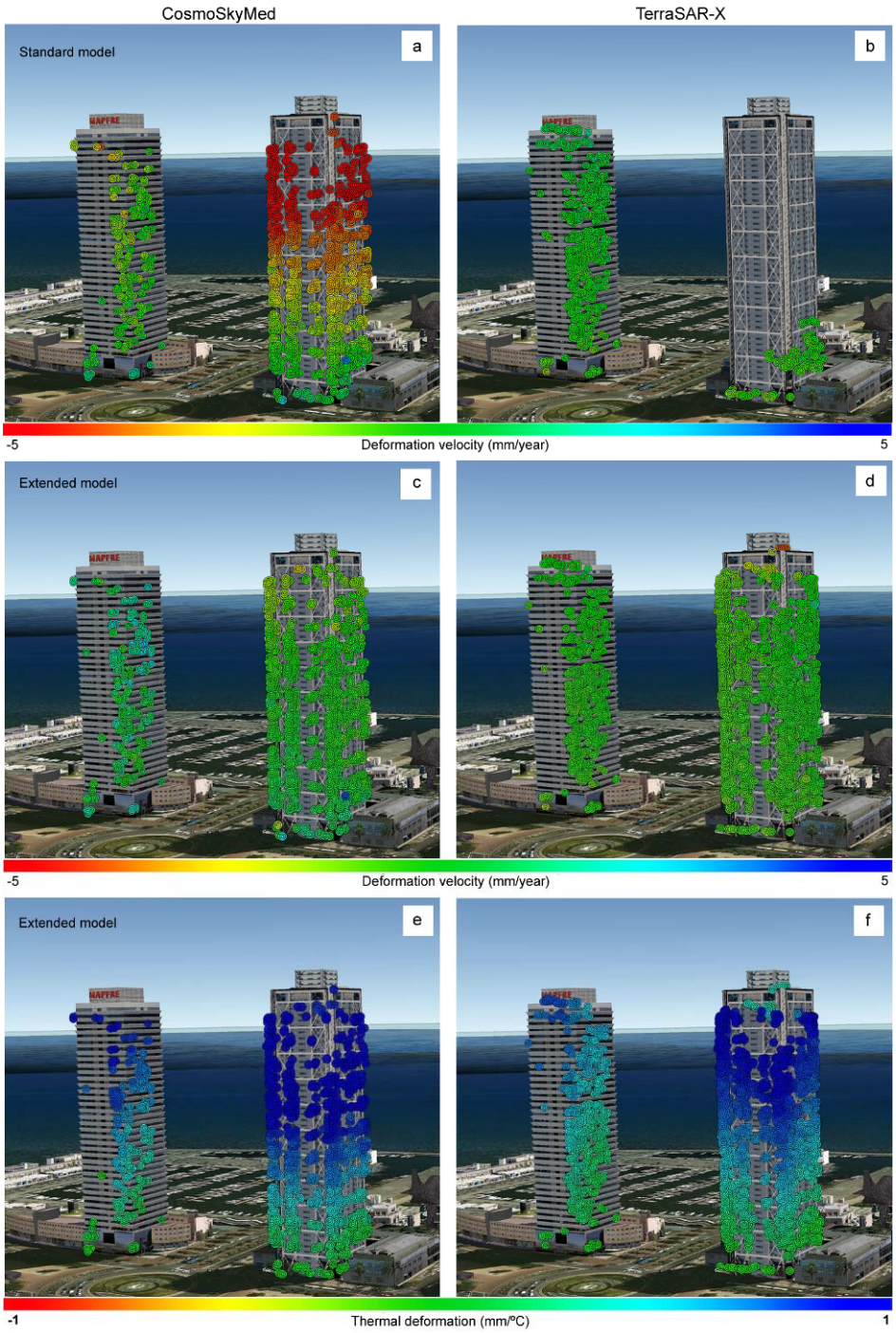

Fig. 4. Geocoded deformation velocity maps estimated from 16 CosmoSkyMed and 28 TerraSAR-X images using the standard PSI model (a, b). Velocity maps (c, d) and thermal maps (e, f) estimated with the extended PSI model. The maps are superimposed over a Google Earth image (© 2013 Google, Institut Cartogràfic de Catalunya).

4. Inter-comparison based on ground-based SAR data

This section describes an experiment where the thermal expansion coefficients estimated from TSX X-band PSI were compared with those derived by Ku-band GBSAR data. The experiment was focused on the skyscraper S_B described in the previous section: 139 GBSAR images were acquired over a 12-h monitoring using an IBIS-L GBSAR manufactured by IDS Spa (www.idscorporation.com). At the same time, thermal camera measurements were performed using the Thermo Tracer TH9100 WR manufactured by NEC, to monitor the temperature of the S_B façades.

The LOS displacement time series were derived from the 139 GBSAR images. The maximum observed LOS displacement is about 13 mm as shown in Fig. 5. It is worth noting that the above displacements were computed by neglecting the atmospheric effects. In fact, we found that the atmospheric effects, in terms of displacement, were below 0.2 mm by using a refractive model (e.g. see Iannini and Guarnieri, 2011) and the measured air humidity, pressure and temperature values.

The analysis was then focused on the data that concern one of the corners of S_B. For a given point of this corner, the Th_{GBSAR} value in the GBSAR LOS was computed as the ratio between its displacement magnitude (estimated from the GBSAR time series) and the temperature variation during the GBSAR campaign. The component related to the horizontal thermal expansion of the observed corner was then subtracted from Th_{GBSAR}. This was deduced from the S_B geometry and assuming a coefficient of thermal expansion of $12 \cdot 10^{-6}$/ºC for this steel structure. Finally, considering the LOS geometry of each point, the remaining Th_{GBSAR} component was projected in the vertical direction, obtaining the Th_V_{GBSAR} value.

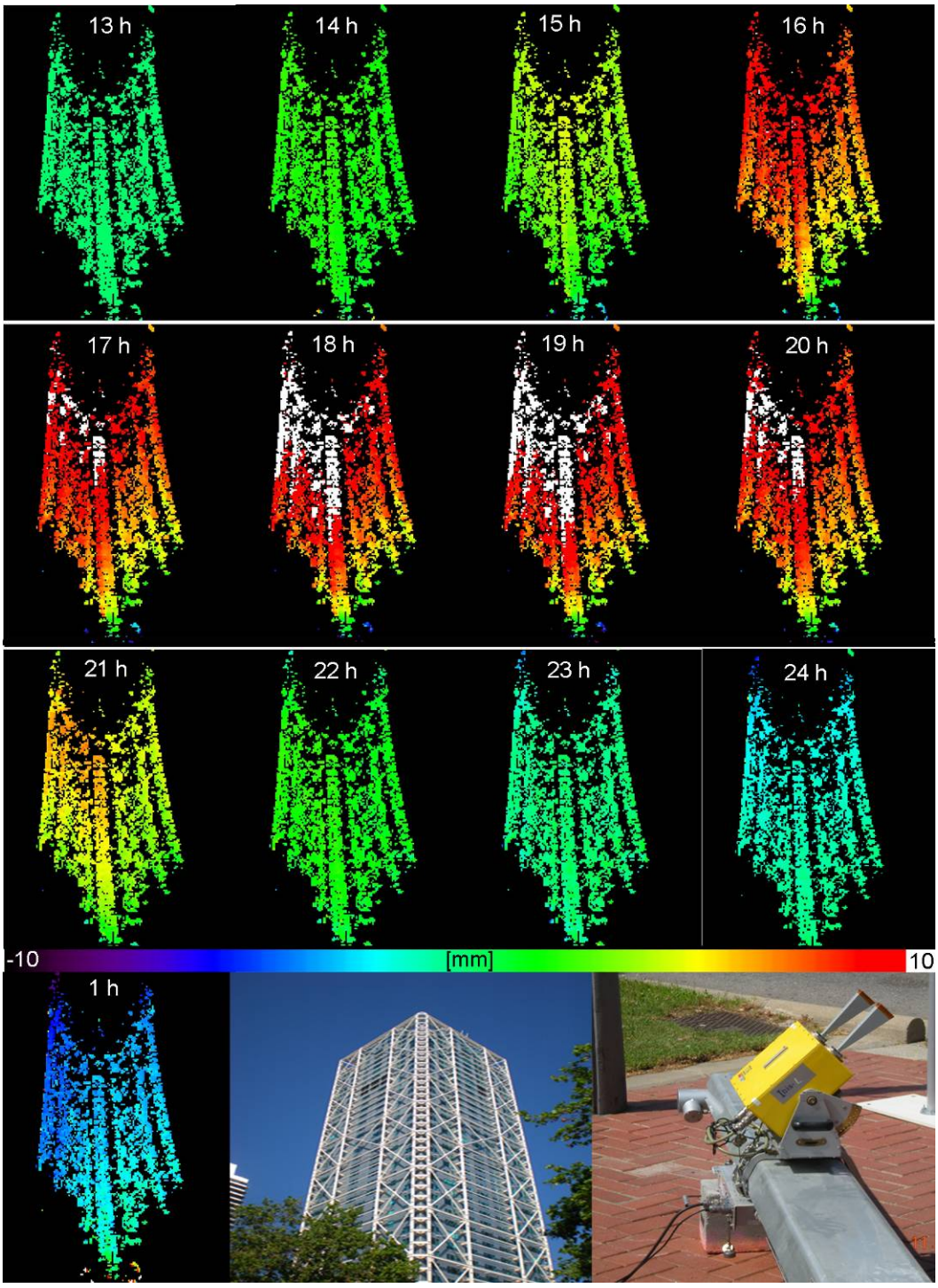

Fig. 5. Maps of accumulated Line-Of-Sight displacements observed from 13 h to 1 h. The displacement values, in [mm], are referred to the 13 h. The colours from green to red and white represent displacements away from the radar sensor, while the colours from green to purple represent displacements toward the sensor. A photograph of the monitored skyscraper (middle) and a photograph of the used GBSAR system (right) are shown at the bottom of the figure.

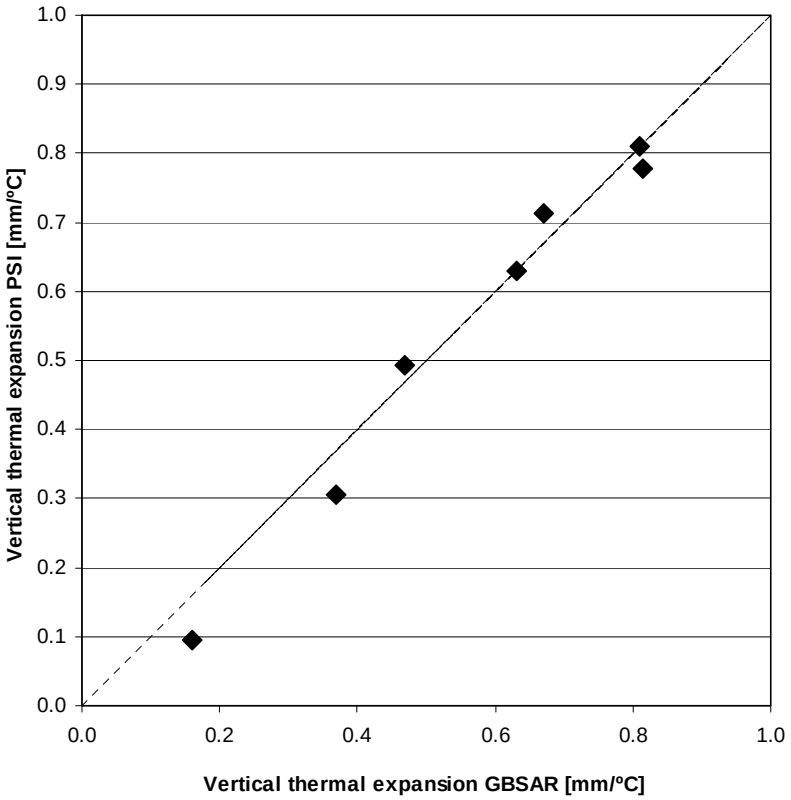

Fig. 6. Scatter plot of the Th_V_{GBSAR} and Th_V_{PSI} values over seven points located on one corner of the skyscraper S_B. The diagonal line represents the perfect agreement between the two sets of estimates.

The TSX PSI estimates, Th_{PSI} , were taken from the data shown in Fig. 4e. The same horizontal thermal expansion component used for the GBSAR estimates was removed, and the remaining component was projected in the vertical direction, getting the Th_V_{PSI} values. Th_V_{GBSAR} and Th_V_{PSI} were then compared, see Fig. 6. There is a good agreement between these values: the maximum absolute difference is 0.07 mm/ºC, the mean is 0.01 mm/ºC and the standard deviation 0.04 mm/ºC. The agreement is remarkable considering that the Th_V estimates were obtained from substantially different procedures. In fact, the Th_V_{GBSAR} was estimated from 12-h observations and using the temperature of the S_B façades, which include the effects of

insolation, while the Th_V_{PSI} comes from 28 observations distributed over two years and by using an average temperature of the city at the time of acquisition of the SAR images.

5. Conclusions

In this paper the capability of X-band PSI to estimate the thermal expansion of buildings and infrastructures has been discussed. Two main issues related to this topic have been addressed. The first one is how to properly model the PSI observations in order to separate the thermal expansion component from the total observed deformation. For this purpose an extended PSI model has been described, which can be used to derive a new PSI product: the map of the thermal expansion parameter or thermal map. The second issue concerns the exploitation of the information contained in the thermal maps. Three examples of thermal maps, concerning a viaduct, a set of industrial buildings and two skyscrapers, have been discussed. The main outcomes are summarized below.

- X-band PSI has a high sensitivity to subtle displacements, including those caused by thermal expansion.
- The thermal maps provide a new type of information, which is related to a physical property of the observed objects (the thermal expansion coefficient) and to their static structure. This has been shown in the example of the viaduct, where a structural static scheme that includes a pinned joint and three slider joints was derived.
- The thermal maps can highlight different thermal expansion behaviours that are related to the type of static structure of the building or infrastructure at hand. This has been shown in the analysis of the two skyscrapers: even though they have the same height, their thermal expansion behaviour is sensibly different.

- If the thermal expansion is not explicitly modelled, the PSI deformation products can be affected by strong distortions, which can be particularly severe if limited PSI datasets in relatively short periods are analysed.
- A weak point of the proposed procedure is given by the problems of parameter estimability, which depend on the number of available SAR images (the larger, the better) and the correlation (the lower, the better) between the vectors $[\Delta T^k]$, $[B_\perp^k]$, $[\Delta Temp^k]$, with k varying from 1 to the N^{th} interferogram. Some of these problems have been illustrated in the case study of the skyscrapers.

Finally, an inter-comparison exercise has been described in the last part of the paper. The thermal expansion coefficients estimated with PSI have been compared with those derived by a Ku-band GBSAR campaign. The good agreement shown by the analysed data confirms the soundness of the proposed PSI procedure.

Acknowledgements

Six of the 28 SAR images used in this work come from the Project "Evaluation of DEM derived from TerraSAR-X data, LAN0634", of the TerraSAR-X Science Service Program. The 16 CosmoSkyMed images used in this work were provided by the Italian Space Agency (ASI), under the CosmoSkyMed AO Project ID 2236. The authors acknowledge Dr. Felipe Buill, Dr. Amparo Nuñez and Dr. Nieves Lantada of the Department of Geotechnical Engineering and Geo-Sciences (ETCG) of the Polytechnic University of Catalonia (UPC) for the thermal camera measurements made during the GBSAR campaign.

References

Bell, J.W., Amelung, F., Ferretti, A., Bianchi, M., Novali, F., 2008. Permanent scatterer InSAR reveals seasonal and long-term aquifer-system response to groundwater pumping and artificial recharge. Water Resour. Res., 44, W02407, doi: 10.1029/2007WR006152.

Bürgmann, R., Hilley, G.E., Ferretti, A., Novali, F., 2006. Resolving vertical tectonics in the San Francisco Bay Area from Permanent Scatterer InSAR and GPS Analysis. Geology 34 (3), 221–224.

Colesanti, C., Le Mouélic, S., Bennani, M., Raucoules, D., Carnec, C., Ferretti, A., 2005. Detection of mining related ground instabilities using the permanent scatterers technique - a case study in the east of France. Int. J. Remote Sens. 26 (1), 201–207.

Crosetto M., Agudo M., Monserrat O., Pucci B. Inter-comparison of persistent scatterer interferometry results. Proceedings of the Fringe 2007 Workshop, 26-30 November 2007, Frascati (Italy). http: earth.esa.int/workshops/fringe07/papers/papers_posters/s7_5cros.pdf.

Crosetto, M., Biescas, E., Duro, J., Closa, J., Arnaud, A., 2008. Generation of Advanced ERS and Envisat Interferometric SAR Products Using the Stable Point Network Technique. Photogramm. Eng. Rem. S. 74 (4), 443–450.

Crosetto, M., Monserrat, O., Iglesias, R., Crippa, B., 2010. Persistent scatterer interferometry: Potential, limits and initial C- and X-band comparison. Photogramm. Eng. Remote Sens. 76 (9), 1061–1069.

Dong, D., Fang, P., Bock, Y., Cheng, M.K., Miyazaki, S., 2002. Anatomy of apparent seasonal variations from GPS-derived site position time series, J. Geophys. Res. 107 (B4), doi: 10.1029/2001JB000573.

Duro, J., Mora, O., Agudo, M., Arnaud, A., 2010. First results of Stable Point Network software using TerraSAR-X data. Proceedings of EUSAR 2010, 7-10 June 2010, Aachen (Germany).

Ferretti, A., Prati, C., Rocca, F., 2000. Nonlinear subsidence rate estimation using permanent scatterers in differential SAR interferometry. IEEE Trans. Geosci. Remote Sens. 38 (5), 2202–2212.

Ferretti, A., Prati, C., Rocca, F., 2001. Permanent scatterers in SAR interferometry. IEEE Trans. Geosci. Remote Sens. 39 (1), 8–20.

Ferretti, A., Perissin, D., Prati, C., Rocca, F., 2005. On the physical nature of SAR permanent scatterers. in Proc. URSI Commission Symp. Microw. Remote Sens. Earth, Oceans, Ice Atmos., Ispra, Italy, 20-21 April 2005.

Ferretti, A., Savio, G., Barzaghi, R., Borghi, A., Musazzi, S., Novali, F., Prati, C., Rocca, F., 2007. Submillimeter Accuracy of InSAR Time Series: Experimental Validation. IEEE Trans. Geosci. Remote Sens. 45 (5), 1142-1153.

Fornaro, G., Reale, D., Verde, S., 2013. Bridge Thermal Dilation Monitoring With Millimeter Sensitivity via Multidimensional SAR Imaging. IEEE Geosci. Remote Sens. Lett., 10 (4), 677–681.

Gernhardt, S., Adam, N., Eineder, M., Bamler, R., 2010. Potential of very high resolution SAR for persistent scatterer interferometry in urban areas. Ann. GIS, 16 (2), 103–111.

Hilley, G.E., Bürgmann, R., Ferretti, A., Novali, F., and Rocca, F., 2004. Dynamics of slow-moving landslides from Permanent Scatterer analysis. Science 304 (5679), 1952–1955.

Iannini, L., Guarnieri, A. M., 2011. Atmospheric phase screen in ground-based radar: statistics and compensation. Geoscience and Remote Sensing Letters, IEEE 8 (3), 537-541.

Merritt, F.S., Loftin, M.K., Ricketts, J.T., 1976. Standard handbook for civil engineers. McGraw-Hill.

Monserrat, O., Crosetto, M., Cuevas M., Crippa B., 2011. The thermal expansion component of Persistent Scatterer Interferometry observations. IEEE Geosci. Remote Sens. Lett. 8, 864–868.

Musson, R. M. W., Haynes, M., and Ferretti, A., 2004. Space-based tectonic modelling in subduction areas using PSInSAR, Seismol. Res. Lett. 75 (5), 598-606.

Perissin, D., Rocca, F., 2006. High-accuracy urban DEM using permanent scatterers. IEEE Trans. Geosci. Remote Sens. 44 (11), 3338-3347.

Raucoules, D., Bourgine, B., De Michele, M., Le Cozannet, G., Closset, L., Bremmer, C., Veldkamp, H., Tragheim, D., Bateson, L., Crosetto, M., Agudo., M., Engdahl, M., 2009. Validation and Intercomparison of Persistent Scatterers Interferometry: PSIC4 project results. Journal of Applied Geophysics 68, 335–347.

Salvi. S., Atzori, S., Tolomei, C., Allievi, J., Ferretti, A., Rocca, F., Prati, C., Stramondo, S., and Feuillet, N., 2004. Inflation rate of the Colli Albani volcanic complex retrieved by the permanent scatterers SAR interferometry technique. Geophys. Res. Lett., 31, L12606, doi: 10.1029/2004GL020253.

Tomás, R., Márquez, Y., Lopez-Sanchez, J.M., Delgado, J., Blanco, P., Mallorquí, J.J., Martínez, M., Herrera, M., Mulas, J., 2005. Mapping ground subsidence induced by aquifer overexploitation using advanced Differential SAR interferometry: Vega Media of the Segura river (SE Spain) case study. Remote Sens. Environ 98, 269–283.